Journal of Physics G:
Nuclear and Particle
Physics

PAPER

Core excitation in ^{92}Mo up to high spin

To cite this article: Vishal Malik *et al* 2025 *J. Phys. G: Nucl. Part. Phys.* **52** 025101

IOP Publishing Journal of Physics G: Nuclear and Particle Physics
J. Phys. G: Nucl. Part. Phys. **52** (2025) 025101 (22pp) https://doi.org/10.1088/1361-6471/ad9343

Core excitation in ^{92}Mo up to high spin

Vishal Malik[1], R Palit[1,*], P C Srivastava[2], P Dey[1], Deepak Patel[2], Biswajit Das[1,3], D Negi[4], U Garg[5], R Raut[6], Nidhi Goel[7], A Kundu[1], A Sindhu[1] and Somnath Nag[7]

[1] Department of Nuclear and Atomic Physics, Tata Institute of Fundamental Research, Mumbai 400005, India
[2] Department of Physics, Indian Institute of Technology Roorkee, Roorkee 247667, India
[3] Department of Radiology and Biomedical Imaging, University of California San Francisco, San Francisco, CA 94143, United States of America
[4] Department of Physics, Manipal Institute of Technology, Manipal Academy of Higher Education, Manipal 576104, India
[5] Department of Physics and Astronomy, University of Notre Dame, Notre Dame, IN 46556, United States of America
[6] UGC-DAE Consortium for Scientific Research, Kolkata Centre, Kolkata 700098, India
[7] Department of Physics, Indian Institute of Technology BHU, Varanasi 221005, India

E-mail: vishal_047@tifr.res.in and palit@tifr.res.in

Received 19 May 2024, revised 8 October 2024
Accepted for publication 15 November 2024
Published 23 December 2024

Abstract

An in-beam gamma-ray spectroscopy study of the even–even nucleus ^{92}Mo has been carried out using the ^{30}Si + ^{65}Cu, ^{18}O + ^{80}Se reactions at beam energies of 120 and 99 MeV, respectively. Angular distribution from the oriented state ratio (R_{ADO}) and linear polarization (Δ_{asym}) measurements have fixed most of the tentatively assigned spin-parity of the high-energy levels. A large-scale shell-model calculation using the GWBXG interaction has been carried out to understand the configuration and structure of both positive and negative parity states up to the highest observed spin. The high-spin states primarily originate from the coupling of excited proton- and neutron-core structures in an almost stretched manner. The systematics of the energy required to form a neutron particle-hole pair excitation, $\nu g_{9/2} \rightarrow \nu d_{5/2}$, is discussed. The lifetimes of a few high-spin states have been measured using the Doppler shift attenuation method. Additionally, a qualitative argument is proposed to explain the comparatively strong E1 transition feeding the 7310.9 keV level.

Keywords: level scheme, shell model, lifetime measurement

1. Introduction

Nuclei in the vicinity of shell closures are of interest in spectroscopic pursuits for probing the various aspects of single-particle as well as collective excitations [1–4] and for testing the applicability of large-basis shell-model calculations. These endeavors have often produced results of impact in the domain of nuclear structure studies. For instance, the low-spin excitations of nuclei around the closure at N ≈50 and with Z ≈40 could be interpreted within the shell-model framework by a model space consisting of $p_{1/2}$ and $g_{9/2}$ orbitals "outside" the ^{88}Sr (Z=38, N=50) core [5–7]. However, for nuclei with N > 49, core-excited configurations are required to be invoked to generate the high-spin states [3, 4, 8–16]. Such (neutron) excitations across the N = 50 shell gap have been reported in ^{86}Kr [8], ^{87}Rb [9], ^{88}Sr [10], ^{89}Y [11], ^{90}Zr [3], ^{91}Nb [17], ^{92}Mo [12, 14], ^{93}Tc [16], ^{94}Ru [16], and ^{85}Rh [16].

The negative-parity band in the high-spin regime has been reported in ^{91}Nb [17], ^{93}Tc [16], and ^{94}Ru [16] nuclei with N = 50 and Z > 40. The underlying dominant configuration for these bands has been identified as $\pi(f_{5/2}^6 p_{3/2}^4 p_{1/2}^1 g_{9/2}^n) \otimes \nu(g_{9/2}^9 d_{5/2}^1)$, with n = 2, 4, and 5 for ^{91}Nb, ^{93}Tc, and ^{94}Ru, respectively. These states are built by the coupling of aligned proton and neutron structures in an almost stretched configuration. Additionally, Huang *et al* [15], in their high-spin study of ^{92}Mo, found new high-energy γ transitions decaying to the 11^- or 12^+ state. These high-energy transitions, with energies ∼2 MeV, have been ascribed to either Z = 38 cross-shell excitation or Z = N = 50 core excitation.

The E1 transitions are strictly forbidden within the $p_{3/2}f_{5/2}p_{1/2}g_{9/2}$ model space in the absence of any pair of orbitals that satisfy the $\Delta l = \Delta j = 1$ condition. The E1 transitions can only underlie the core-breaking excitations either from the $f_{5/2}$ and $p_{3/2}$ orbitals to the $g_{7/2}$ and $d_{5/2}$ orbitals, across the gap at N, Z = 50, or from the $f_{7/2}$ orbital to the $g_{9/2}$ orbital across the gap at N, Z = 28. These transitions are generally quite weak and known to be characterized by B(E1) ∼ 10^{-5} W.u. [18, 19]. However, in ^{94}Ru, an enhancement in the B(E1) by a factor of 100 has been observed [18] and ascribed to the involvement of proton and neutron core excitation. It is worth probing such enhancements in other neighboring nuclei, such as ^{92}Mo, wherein evidence of core excitations has already been reported in earlier studies [15].

This paper reports on experimental reinvestigation of the level structure of ^{92}Mo along with large-basis shell-model calculations of the observed/known levels therein. In addition, lifetime measurements have been carried out for some of the high-spin states using the Doppler shift attenuation method (DSAM) with the aim to probe the associated transition probabilities. The goal was to look for possible enhancements of the same, particularly for the E1 transitions that are known to underlie the core excitations for these (Z > 40, N ∼50) nuclei.

2. Experimental details and data analysis

The excitation scheme of ^{92}Mo was probed in two experiments at Pelletron Linac Facility (PLF) in TIFR, Mumbai. High-spin states of ^{92}Mo were produced by ^{65}Cu(^{30}Si,p2n) and ^{80}Se(^{18}O,6n) reactions at a beam energy of 120 MeV and 99 MeV, respectively. Here, ^{30}Si and ^{18}O beams were bombarded on 1 mg cm^{-2} thick ^{65}Cu with 6.5 mg cm^{-2} ^{197}Au backing and on 1.4 mg cm^{-2} ^{80}Se with a backing of 1.5 mg cm^{-2} ^{27}Al, respectively. The gamma rays emitted from the residual excited nuclei were detected by the Indian National Gamma Array [20] setup in TIFR, Mumbai. The array consisted of 15 and 13 Compton suppressed HPGe clover detectors during the experiment with the ^{65}Cu target and the ^{80}Se target, respectively. In the ^{65}Cu experiment, three detectors were placed at 157°, 140°, 115°, 40°, and 90 ° with

respect to the beam direction. And in the ^{80}Se experiment, three detectors were positioned at 157° and 140°, two at 115°, four at 90°, and one at 65°. The data were collected using XIA-based digital data acquisition with two- or higher-fold trigger conditions. The collected data were sorted offline using the Multi pARameter time-stamped-based COincidence Search (MARCOS) code [21], developed at TIFR, to generate the E_γ-E_γ matrix and E_γ-E_γ-E_γ cube, as well as asymmetric angle dependent polarization and angular distribution from the oriented state (ADO) matrices for γ-γ coincidence time windows (ΔT) of 500 ns and 2000 ns. Approximately, 1.4×10^{10} and 2.6×10^{9} with two- or higher-fold coincidence events were recorded in the experiment with the ^{65}Cu and ^{80}Se targets, respectively. The analysis of the sorted data was carried out using Radware software [22, 23]. The data from the reaction with the ^{65}Cu target were primarily used to construct the level scheme due to the higher population of ^{92}Mo therein, while data from the ^{80}Se target were used to determine the lifetimes of a few states in ^{92}Mo using the DSAM [24, 25].

Energy and efficiency calibration of the setup was carried out using the EuBa source. The multipolarity of the γ-ray was assigned using angular distribution from the oriented state ratio ($R_{\rm ADO}$). Two asymmetric matrices were formed with y-axes using the γ-rays at all angles and x-axes as the coincidence γ-rays detected by the 157° and 90° detectors, respectively. The ADO ratio was determined from [26]

$$R_{\rm ADO} = \frac{I_\gamma(157°)}{I_\gamma(90°)} \tag{1}$$

where I_γ is the intensity of a γ-ray at the respective angle (157° or 90°, indicated in the parentheses) in coincidence with a γ-ray detected at any angle. Previously known stretched quadrupole and dipole transitions from the ^{90}Mo [27], ^{89}Nb [28], ^{89}Zr [29], ^{88}Zr [30], ^{91}Mo [31], ^{91}Nb [17], and ^{92}Mo [13] were used to benchmark the $R_{\rm ADO}$ values. The same turned out to be ∼1.6 and ∼0.7 for stretched quadrupoles and stretched dipoles, respectively.

The polarization method was used to assign the parity of the states. The 'integrated polarization by directional correlation of oriented states' method was used to fix the parity of radiation. The parallel or perpendicular scattered γ-rays in the 90° clovers' crystals were used to distinguish between the electric or magnetic character of the radiation. The polarization asymmetry defined as [32]

$$\Delta_{\rm asym} = \frac{a(E_\gamma)N_\perp - N_\parallel}{a(E_\gamma)N_\perp + N_\parallel} \tag{2}$$

was used for polarization measurement. Here, $\Delta_{\rm asym}$ is the polarization asymmetric parameter, $N_\parallel$ and $N_\perp$ are the number of parallel and perpendicular scattered γ-rays with respect to the reaction plane, and $a(E_\gamma)$ is the inherent geometrical asymmetry of the detection system. The $N_\perp$ and $N_\parallel$ were extracted from the asymmetric matrices constructed for this purpose. These had γ-rays detected by the perpendicular (parallel) combination of crystals, in the detectors at 90°, on the X-axis and the coincident γ-rays detected at all other angles on the Y-axis. The $a(E_\gamma)$ was determined from $a(E_\gamma)=\frac{(N_\parallel)_{\rm unpolarized}}{(N_\perp)_{\rm unpolarized}}$ for γ-rays from (unpolarized) EuBa radioactive sources and by fitting the $a(E_\gamma)$ data with the polynomial $a(E_\gamma)=A + BE_\gamma$. The values of A and B were found to be $A = +0.973(3)$ and $B = +2.5(5) \times 10^{-5}$ keV^{-1}. The positive (negative) value of $\Delta_{\rm asym}$ indicates the electric (magnetic) character for stretched transitions.

The lifetimes of a few selected high-spin states of the ^{92}Mo nucleus were determined using the DSAM. The associated analysis was carried out using both the conventional LINESHAPE package, of Wells and Johnson [24] and the modifications/developments, as reported in [25].

The above two programs differ in the choice of stopping powers used to simulate the trajectories of the (^{92}Mo) residues through the target and the backing media. The stopping powers in the analysis using the conventional LINESHAPE were calculated using the algorithm of Northcliffe and Schilling [24], while those in the modified version used the SRIM [33] code. The simulated trajectories (for 10 000 residues), as viewed by the detectors at different angles, were used to calculate the respective Doppler shapes that were least-squares fitted to the corresponding experimental spectra to extract the level lifetimes. The details of the lifetime analysis using the LINESHAPE package can be found in a number of papers, such as [34–36].

3. Results

The level scheme of the ^{92}Mo nucleus, following the current study, is illustrated in figure 1. Intensity balances, energy sums, and coincidence conditions were used to build the level scheme of ^{92}Mo. In addition to previously reported γ rays, nine new gamma transitions are observed in this work (figure 1). The intensities of 1510.2-, 772.9- (after correcting for newly observed 774.9 keV transition), and 244.0 keV transitions were measured from the total projection spectrum, and all the other γ-ray intensities were normalized to the most intense 1510.2 keV transition. Figures 2 and 3 show the γ gated spectrum, which is generated from the matrix and cube for a 500 ns time window. The spectra illustrate both confirmed transitions reported earlier and newly observed transitions (shown in red for easy identification). The 8^+ is an isomer state with a half-life of $T_{1/2}$=190(3) ns [37]. The intensities of 329.5-, 2361.0-, 649.6-, and 1075.1keV transitions were calculated using a matrix generated from a 2000 ns time window. In the present work, the spin-parity of most of the energy levels is fixed. Earlier polarization measurement for the ^{92}Mo nucleus was reported by Pattababiraman *et al* [13]. However, the polarization results of the present work differed from the same for 244.0-, 1097.4-, 2064.4-, and 472.1keV (see figure 4) transitions. We carried out Δ_{asym} measurements for each of these transitions in different possible gates and all the Δ_{asym} values obtained were consistent with each other. Typical parallel and perpendicular Compton scattering spectra in 90° detectors for 2064.4-, 234.6-, 799.9-, 1510.2-, 536.8, and 2047.6 keV transitions are shown in figure 4. The discussions on the observed level scheme, hereafter, have been arranged by dividing it into three parts, i.e. Band I, Band II, and additional states. These are followed by discussions on the lifetime measurements for selected states of the nucleus.

3.1. Band I

The states at 9358.6-, 10 019.6-, 10 578.4-, and 11 215.3 keV energy are included in this band. These states were earlier reported in [13, 15]. However, their spin-parity was only tentative therein. The E2 nature of the 2047.6 keV γ-ray transition (see figures 4 and 5), following the present analysis, has changed the spin-parity assignment of the 9358.6 keV level to 16^+ and, accordingly, that of the other states of the band [13, 15]. We could not extract the polarization asymmetry of the 2225.1 keV transition. We found a new transition, 774.9 keV. The R_{ADO} value is indicative of the dipole nature of the 774.9 keV transition. However, due to poor statistics of polarization data, the parity of the 8085.9 keV state could not be assigned. Additionally, we found two transitions decaying out of Band I, and feeding the 8085.9 keV level. The 1272.5 keV ($16^+ \rightarrow 15^+$) has been newly identified in this work, while the 1933.8 keV ($17^+ \rightarrow 15^+$) transition was reported in [13], albeit with a different placement that has been modified following the present analysis. Moreover, we found two new high-energy transitions (figures 2 and 3) with energies of 1879.1 and 2030.9 keV

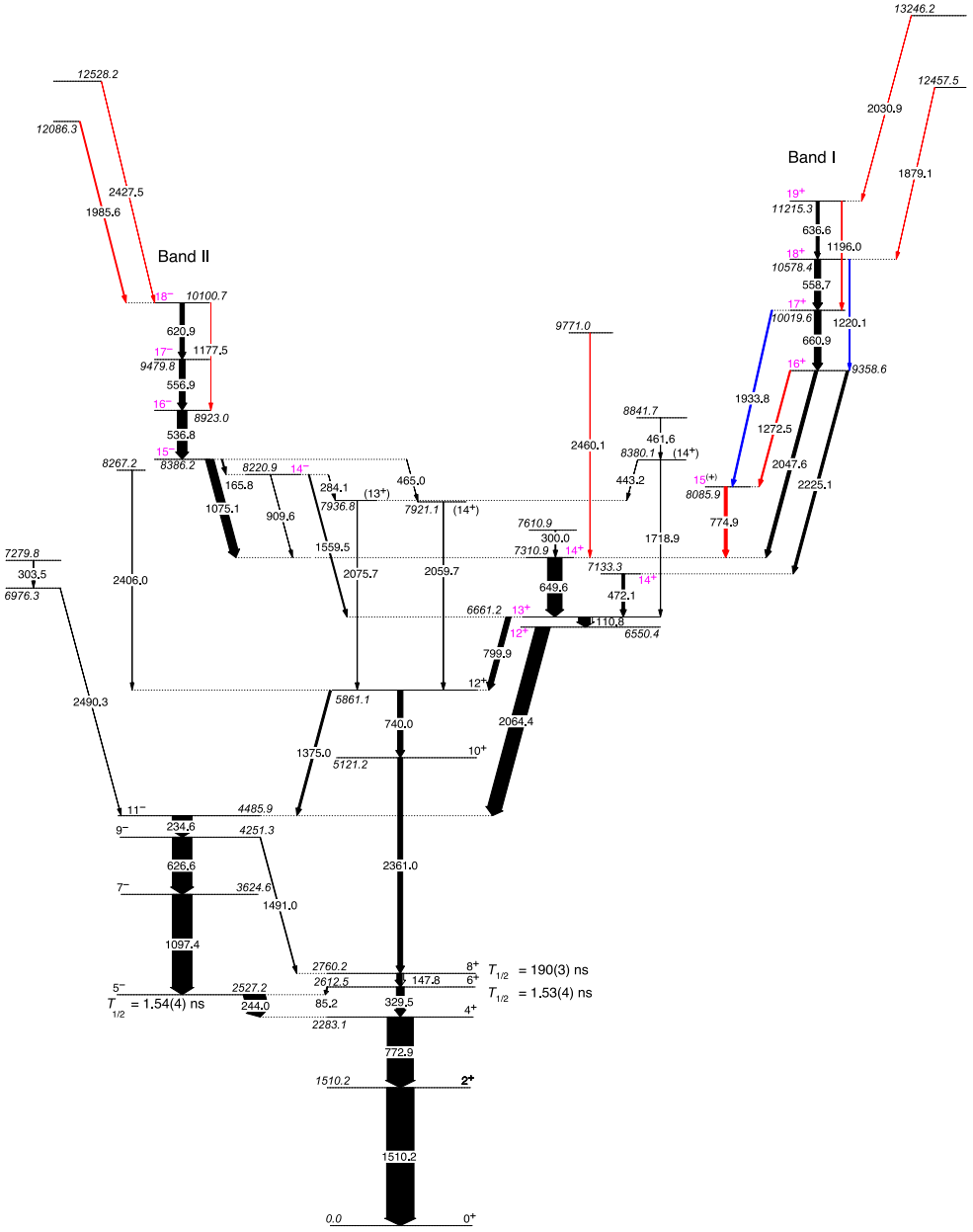

Figure 1. The proposed partial level scheme for ^{92}Mo from the present work. The red and blue colors represent new and rearranged transitions, respectively. The magenta color indicates the confirmed spin-parity of the states that were either tentatively assigned earlier or have been changed based on the present work. All shown energies are in keV. The half-lives, $T_{1/2}$, of the isomers shown were adopted from [37]. The thickness of the arrow represents the intensity of γ-transitions, as mentioned in table 1. The energies of all the levels were estimated using the GTOL fitting code developed by National Nuclear Data Center (NNDC).

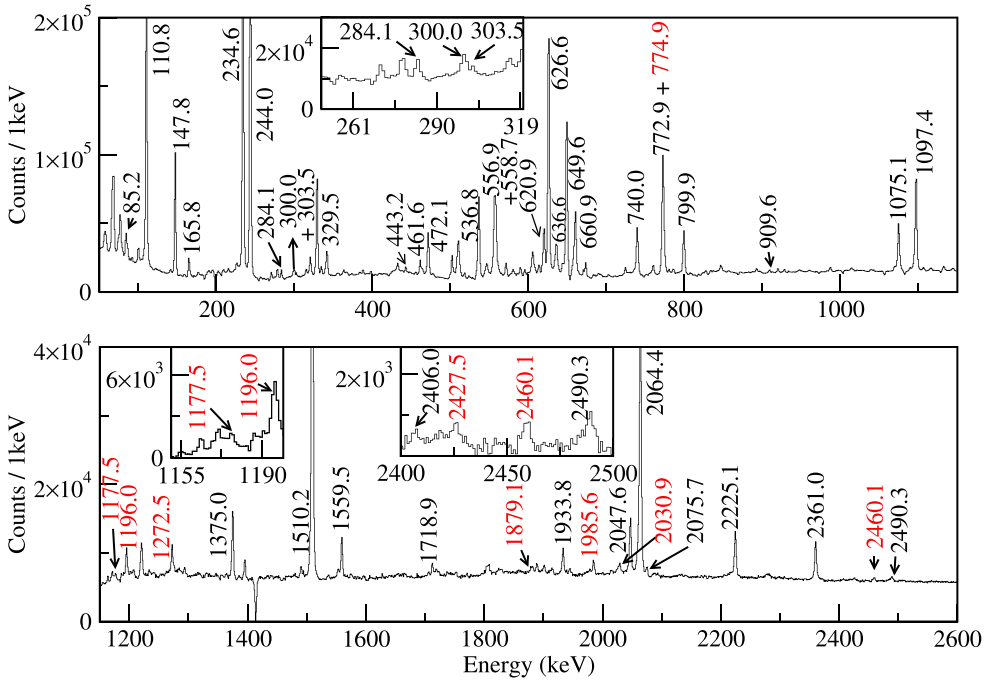

Figure 2. Representative sums of γ gated spectra with gates on 772.9-, 1097.4-, and 2361.0 keV (time window=$\pm$ 500 ns). Newly observed transitions are labeled in red.

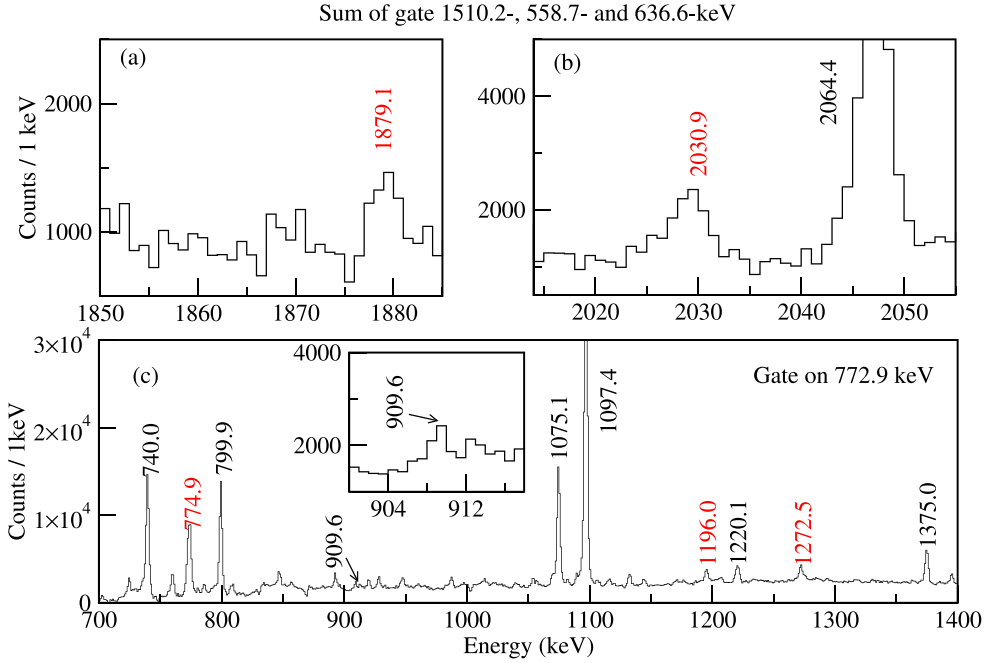

Figure 3. (a), (b) Representative sums of γ gated spectra with gates on 1510.2, 558.7-, and 636.6 keV (time window = $\pm$ 500 ns). (c) The coincidence spectrum from the gate on the 772.9 keV γ transition (time window = $\pm$ 500 ns).

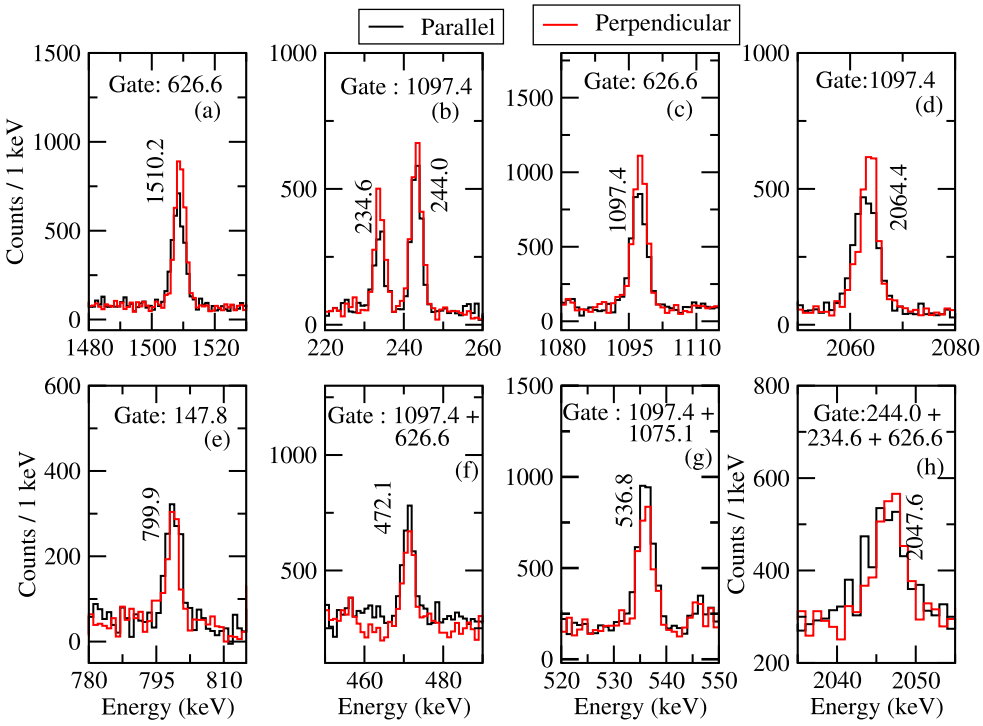

Figure 4. Representative examples of (a), (c) 626.6-, (b), (d) 1097.4-, (e) 147.8-, (f) 1097.4 + 626.6-, (g) 1097.4 + 1075.1-, and (h) 244.0 + 234.6 + 626.6 keV gated spectra of parallel and perpendicular Compton scattering in 90° clover detectors. Higher counts for 1510.2, 234.6, 244.0, 1097.4, 2064.4, and 2047.6 keV transitions in the perpendicular scattered spectrum indicate its electric character, and the reverse condition suggests the magnetic nature of 799.9, 472.1, and 536.8 transitions.

decaying to 18^+, and 19^+ states of Band I, respectively. However, these were plagued with insufficient counts in the angle gated spectra and could not be analyzed for R_{ADO} or polarization asymmetry.

3.2. Band II

Levels at 8386.2-, 8923.0-, 9479.8-, and 10 100.7 keV are included in this band. The sequence of strong M1 γ transitions may hint at the presence of magnetic rotation. This band has been observed in earlier work too [12, 13, 15], where its parity was tentatively assigned to positive. Our polarization measurement fixed the parity of this band to negative, conflicting with the previously tentative assignment. We observed a new crossover transition, 1177.5 keV (see level scheme 1), connecting the 18^- and 16^- states. Additionally, as in Band I, we observed two new high-energy transitions, 1985.6 and 2427.5 keV (figure 2). They were placed on top of the 10 100.7 keV energy level.

3.3. Additional states

There are states that have been observed in this study but that have not been discussed in the aforementioned contexts of Bands I and II, and for which the parity assignments have been modified from the previously reported ones.

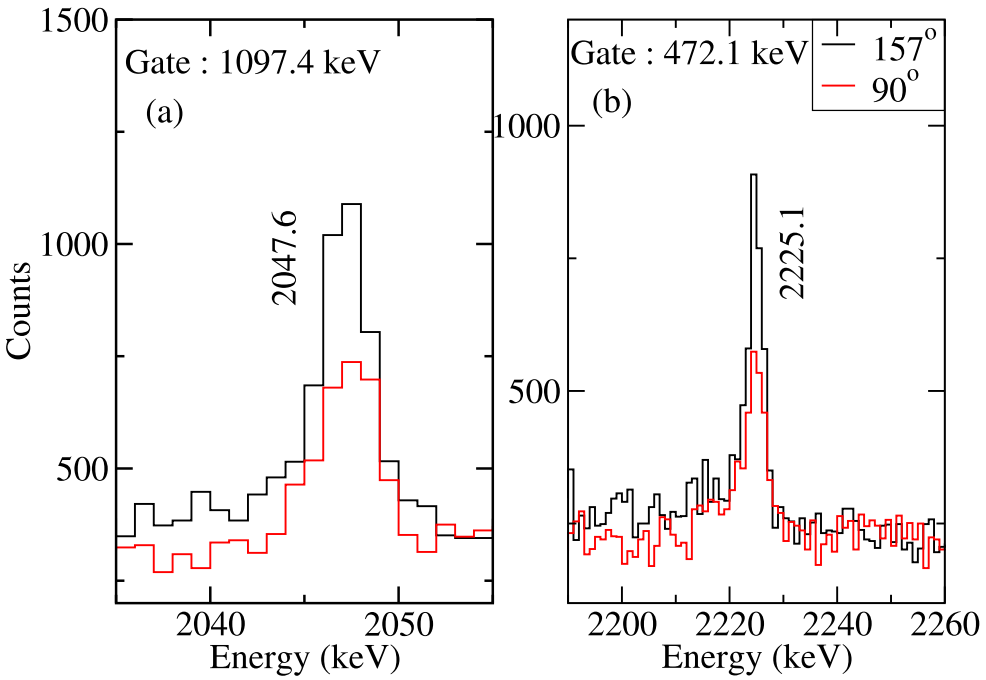

Figure 5. Representative spectra of 157°, 90° detectors generated using a gate on (a) 1097.4 and (b) 472.1 keV transitions. The estimated R_{ADO} values for 2047.6 and 2225.1 keV transitions are 1.62(9) and 1.59(7), respectively, suggesting a quadrupole nature conflicting with the previously tentative assignments [14, 15].

Polarization asymmetry of 2064.4-, 799.9-, 649.6-, 1559.5-, and 1075.1 keV γ-ray transitions has been extracted in multiple gates, was observed to be consistent, and the quoted value (see table 1) is the weighted average of these individual values. The 799.9-, 2064.4-, and 472.1 keV transitions were previously assigned as E1, M1, and E1, respectively [13, 15]. However, in our multipolarity measurements, we identified these transitions as M1, E1, and M1, respectively. The 649.6keV transition, however, was found to have the same multipolarity as reported in [13, 15]. These measurements led to a change in the parity of the 6550.4-, 6661.2-, and 7310.9 keV energy levels from negative to positive. In [13, 15], the 7133.3- and 6661.2keV levels were assigned as 14^{+} and 13^{-}, respectively, assuming the 472.1 keV transition was E1 in nature. Since we have reassigned the spin-parity of the 6661.2 keV level to 13^{+} and identified the 472.1 keV transition as M1, this change does not affect the spin-parity of the 7133.3 keV state. Likewise, the E1 nature of 1559.5-, and 1075.1 keV transitions led to modification of the 8220.9- and 8386.2 keV energy levels from tentative positive to negative.

We confirmed the 2490.3-, 303.5-, 2406.0-, 2075.7-, 2059.7-, 284.1-, 465.0-, 165.8-, and 300.0 keV transitions reported by Z Huang *et al* in [15]. However, despite sufficient statistics in the experimental spectra, we did not observe the 620.6-, 111.9-, 775.1-, 656.5-, 2614.0keV γ rays reported in [15].

3.4. Lifetime measurement

Figures 6 and 7 illustrate the representative fits of the observed Doppler shapes for some of the transitions. In figure 6, the spectra were generated using a gate on the 244.0 keV

Table 1. The level energy (E_i) and spin-parity of the states, as well as the γ-ray energy (E_γ), intensity (I_γ), R_{ADO}, Δ_{asym}, and multipolarity of the transitions obtained in this study. The quoted errors are due to fitting, background subtraction, and efficiency correction.

E_γ[a] (keV)	Level energy (E_i) (keV)	Intensity (I_γ)	R_{ADO}	Polarization asym. (Δ_{asym})	Multipolarity	$I_i^\pi \longrightarrow I_f^\pi$
1510.2	1510.2(3)	100.0(9)	1.64(3)[b]	+0.07(1)	E2	$2^+ \rightarrow 0^+$
772.9	2283.1(5)	94.6(18)	1.44(2)[b]	+0.05(1)	E2	$4^+ \rightarrow 2^+$
244.0	2527.2(5)	72.5(29)	0.82(5)[b]	+0.05(2)	E1	$5^- \rightarrow 4^+$
329.5	2612.5(5)	26.1(21)	1.44(7)[b]	+0.11(2)	E2	$6^+ \rightarrow 4^+$
85.2	2612.5(5)	3.0(4)				$6^+ \rightarrow 5^-$
147.8	2760.2(6)	19.3(20)	1.74(15)[b]		Quadrupole	$8^+ \rightarrow 6^+$
1097.4	3624.6(6)	71.7(55)	1.61(2)[b]	+0.07(1)	E2	$7^- \rightarrow 5^-$
626.6	4251.3(6)	70.8(55)	1.72(3)[b]	+0.08(1)	E2	$9^- \rightarrow 7^-$
1491.0	4251.3(6)	2.3(2)				$9^- \rightarrow 8^+$
234.6	4485.9(7)	68.4(59)	1.85(12)[b]	+0.15(2)	E2	$11^- \rightarrow 9^-$
2361.0	5121.2(7)	17.6(20)	1.65(17)[b]	+0.04(3)	E2	$10^+ \rightarrow 8^+$
740.0	5861.1(7)	19.2(2.2)	1.41(4)[b]	+0.12(2)	E2	$12^+ \rightarrow 10^+$
1375.0	5861.1(7)	7.5(8)				$12^+ \rightarrow 11^-$
2064.4	6550.4(7)	51.7(58)	0.76(2)[b]	+0.03(1)	E1	$12^+ \rightarrow 11^-$
110.8	6661.2(7)	42.6(56)	0.94(8)[b]		Dipole	$13^+ \rightarrow 12^+$
799.9	6661.2(7)	18.6(21)	0.81(3)[b]	−0.13(2)	M1	$13^+ \rightarrow 12^+$
2490.3	6976.3(9)	0.71(1)				$\rightarrow 11^-$
472.1	7133.3(7)	9.4(11)	0.67(3)[b]	−0.12(3)	M1	$14^+ \rightarrow 13^+$
303.5	7279.8(11)					
649.6	7310.9(7)	52.8(60)	0.58(1)[b]	−0.10(2)	M1	$14^+ \rightarrow 13^+$
300.0	7610.9(9)	3.1(4)				$\rightarrow 14^+$
2059.7	7921.1(8)	2.3(3)				$(14^+) \rightarrow 12^+$
2075.7	7936.8(8)	1.3(6)				$(13^+) \rightarrow 12^+$
774.9	8085.9(8)	10.7(13)	0.67(12)[b]		Dipole	$15^{(+)} \rightarrow 14^+$
284.1	8220.9(7)					$14^- \rightarrow (13^+)$
1559.5	8220.9(7)	4.0(5)	0.62(8)[b]	+0.04(4)	E1	$14^- \rightarrow 13^+$
909.6	8220.9(7)					$15^- \rightarrow 14^+$
2406.0	8267.2(9)					$\rightarrow 12^+$

Table 1. (Continued.)

E_γ[a] (keV)	Level energy (E_i) (keV)	Intensity (I_γ)	R_{ADO}	Polarization asym. (Δ_{asym})	Multipolarity	$I_i^\pi \longrightarrow I_f^\pi$
1718.9	8380.1(8)					$(14^+) \rightarrow 13^+$
443.2	8380.1(8)					$(14^+) \rightarrow (13^+)$
165.8	8386.2(7)	3.9(5)	1.03(17)[b]		Dipole	$15^- \rightarrow 14^-$
465.0	8386.2(7)					$15^- \rightarrow (14^+)$
1075.1	8386.2(7)	29.8(34)	0.77(2)[b]	+0.05(2)	E1	$15^- \rightarrow 14^+$
461.6	8841.7(10)					$\rightarrow (14^+)$
536.8	8923.0(8)	28.1(32)	0.59(2)[b]	−0.13(2)	M1	$16^- \rightarrow 15^-$
2047.6	9358.6(8)	11.8(14)	1.62(9)[b]	+0.04(5)	E2	$16^+ \rightarrow 14^+$
1272.5	9358.6(8)	4.5(6)	0.54(5)[b]		Dipole	$16^+ \rightarrow 15^+$
2225.1	9358.6(8)	9.1(11)	1.59(7)[b]		Quadrupole	$16^+ \rightarrow 14^+$
556.9	9479.8(9)	21.4(25)	0.62(2)[b]	−0.11(3)	M1	$17^- \rightarrow 16^-$
2460.1	9771.0(9)	0.6(1)				$\rightarrow 14^+$
660.9	10 019.6(8)	24.0(30)	0.57(2)[b]	−0.12(2)	M1	$17^+ \rightarrow 16^+$
1933.8	10 019.6(8)	5.1(7)	1.47(10)[b]		Quadrupole	$17^+ \rightarrow 15^+$
620.9	10 100.7(9)	16.3(19)	0.52(2)[b]	−0.11(3)	M1	$18^- \rightarrow 17^-$
1177.5	10 100.7(9)					$18^- \rightarrow 16^-$
558.7	10 578.4(8)	22.4(29)	0.71(3)[b]	−0.11(5)	M1	$18^+ \rightarrow 17^+$
1220.1	10 578.4(8)					$18^+ \rightarrow 16^+$
636.6	11 215.3(9)	10.8(14)	0.59(6)[b]	−0.14(4)	M1	$19^+ \rightarrow 18^+$
1196.0	11 215.3(9)	2.6(3)				$19^+ \rightarrow 17^+$
1985.6	12 086.3(11)	3.3(4)				$\rightarrow 18^-$
1879.1	12 457.5(10)					$\rightarrow 18^+$
2427.5	12 528.2(11)					$\rightarrow 18^-$
2030.9	13 246.2(11)	0.8(1)				$\rightarrow 19^+$

[a] The uncertainties of γ-ray energy centroids of strong ($I_\gamma \geqslant 10$) and weak ($I_\gamma < 10$) transitions are around 0.3 and 0.6 keV, respectively.
[b] Calculated using quadrupole and dipole gates, respectively.

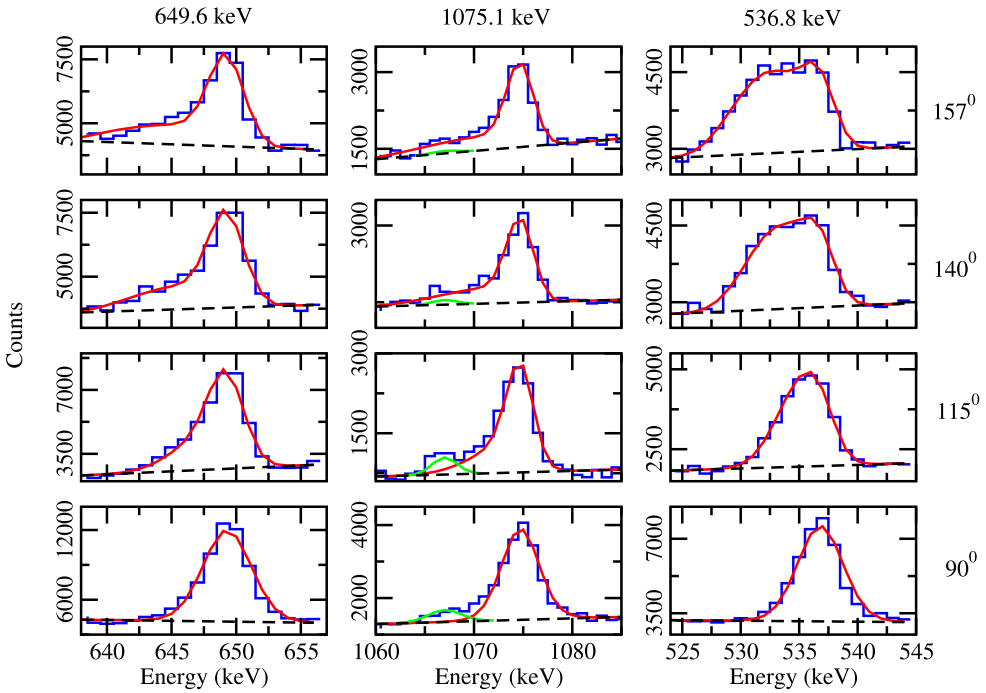

Figure 6. Spectra generated using a gate on the 244.0 keV transition along with the simulated lineshape in different angles. The top transition, 536.8 keV, was assumed to have 100% side feeding. The measured lifetime is shown in table 2. The spectra corresponding to the leftmost, middle, and rightmost panels are for the 649.6-, 1075.1-, and 536.8 keV transitions, respectively. The red curve represents the lineshape fitting and green curve represents the stopped peak.

transition. The top transition, i.e. 536.8 keV, was fitted assuming 100% side feeding. For the 556.9 keV transition, it is necessary to use a gated spectrum which does not include the 558.7 keV transition. Therefore, the spectra in figure 7 were generated using a gate on the 1075.1 keV transition. Similarly, the topmost transition was lineshape fitted by assuming 100% side feeding. The side feeding was modeled with independent feeder states for individual levels. The measured mean and effective lifetimes are shown in table 2. The earlier lifetime study by Das *et al* [38] provided an upper limit on the mean lifetime of 14^{+}, 15^{-}, 16^{-}, and 17^{-} of 2 ps. The present results are noted to be within the same limit. However, we were unable to perform a lifetime measurement of the 620.9 keV transition due to the nearby strong 626.6 keV transition.

4. Shell-model calculations and discussion

The shell-model calculation was performed using the GWBXG effective interaction [39–42] with a ^{68}Ni core. The GWBXG interaction has $1f_{5/2}$, $2p_{3/2}$, $2p_{1/2}$, and $1g_{9/2}$ proton orbitals and $2p_{1/2}$, $1g_{9/2}$, $1g_{7/2}$, $2d_{5/2}$, $2d_{3/2}$, and $3s_{1/2}$ neutron orbitals. The single-particle energies (in MeV) used in this interaction are $1f_{5/2} = -5.322$, $2p_{3/2} = -6.144$, $2p_{1/2} = -3.941$, and $1g_{9/2} = -1.250$ for the proton orbitals, and $2p_{1/2} = -0.696$, $1g_{9/2} = -2.597$, $1g_{7/2} = +5.159$, $2d_{5/2} = +1.830$, $2d_{3/2} = +4.261$, and $3s_{1/2} = +1.741$ for the neutron orbitals.

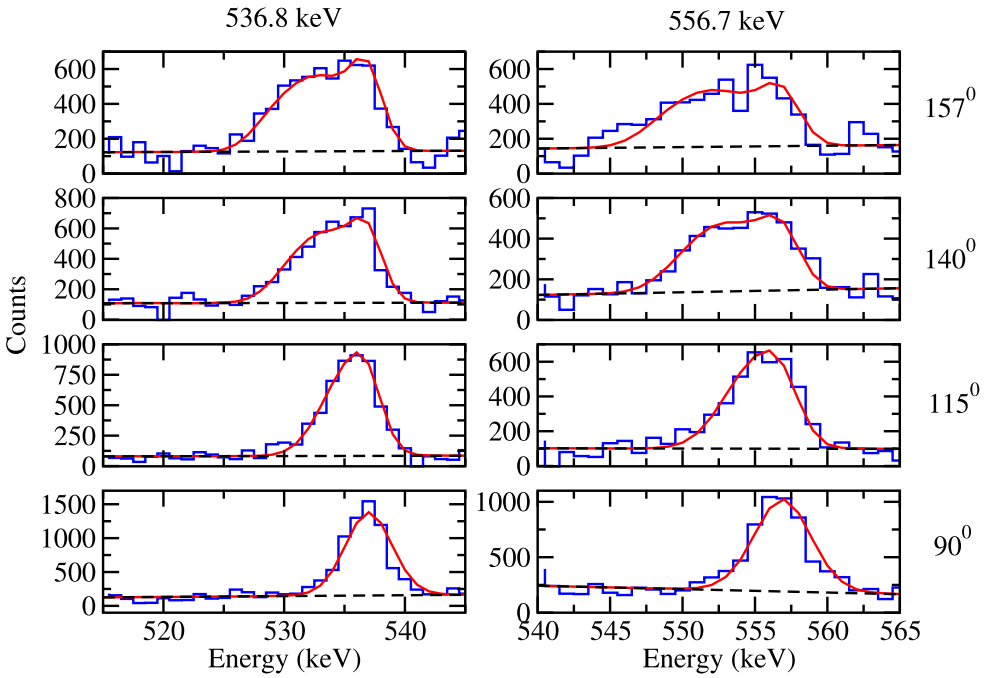

Figure 7. Spectra generated using a gate on the 1075.1 keV transition along with the simulated lineshape in different angles. The top transition, 556.9 keV, was assumed to have 100% side feeding. The measured lifetime is shown in table 2 The spectra corresponding to the leftmost and rightmost panels are for the 536.8- and 556.8 keV transitions, respectively.

We applied a $1p-1h$ excitation across a neutron shell of $N=50$. We allowed one neutron to occupy any of the $\nu(g_{7/2})$, $\nu(d_{5/2})$, $\nu(d_{3/2})$, and $\nu(s_{1/2})$ orbitals, while no truncation was employed for the proton orbitals $f_{5/2}$, $p_{3/2}$, $p_{1/2}$, and $g_{9/2}$. We used the KSHELL [43] shell-model code for the calculation. The theoretically predicted positive- and negative-parity states are shown in tables 3–5. A comparison of experimental levels and shell-model calculated levels using GWBXG interaction is shown in figure 8. Only those experimental energy levels are shown in figure 8 whose spin is at least confirmed, and tentatively assigned levels are discussed in the text.

4.1. Positive-parity states

The theoretical calculation suggests the ground state mainly comes from $\pi(f_{5/2}^6p_{3/2}^4p_{1/2}^2g_{9/2}^2)\otimes\nu(g_{9/2}^{10})$ mixed with $\pi(f_{5/2}^6p_{3/2}^4p_{1/2}^0g_{9/2}^4)\otimes\nu(g_{9/2}^{10})$ and $\pi(f_{5/2}^6p_{3/2}^2p_{1/2}^2g_{9/2}^4)\otimes\nu(g_{9/2}^{10})$ configurations. The shell-model predicted 2^+ state primarily stems from $\pi(f_{5/2}^6p_{3/2}^4p_{1/2}^0g_{9/2}^4)\otimes\nu(g_{9/2}^{10})$ and $\pi(f_{5/2}^6p_{3/2}^4p_{1/2}^2g_{9/2}^2)\otimes\nu(g_{9/2}^{10})$ mixed with $\pi(f_{5/2}^4p_{3/2}^4p_{1/2}^2g_{9/2}^4)\otimes\nu(g_{9/2}^{10})$. The theoretical B(E2) values for the transitions $4_1^+\rightarrow2_1^+$ and $4_2^+\rightarrow2_1^+$, using $e_p=1.5e$ and $e_n=0.5e$, are 0.1 and 412.2 e^2fm^4, respectively. This essentially indicates that the $4_1^+\rightarrow2_1^+$ transition is prohibited. On the other hand, as indicated in [44], seniority is partially conserved in the $\pi g_{9/2}$ shell for $N=50$ nuclei, reflecting almost pure $\nu=2$ states. The 4_2^+ state has a $\nu=4$ configuration with a weightage of 17.8%, but the 4_1^+ state is nearly pure, with ν=2. This led us to interpret the

Table 2. The lifetimes and B($\sigma\lambda$) of states in ^{92}Mo.

E_γ (keV)	$I_i^\pi \rightarrow I_f^\pi$	Mean (τ) lifetime (ps)	Effective lifetime (τ_{eff}) (ps)	Side-feeding lifetime (τ_s) (ps)	Theoretical lifetime (τ_{th}) (ps)	Expt. B($\sigma\lambda$) (W.u.)	Theoretical B($\sigma\lambda$) (W.u.)
649.6	$14^+ \rightarrow 13^+$	$0.68^{+0.03}_{-0.03}$		0.21(1)	1.22	0.17(1)	0.02
1075.1	$15^- \rightarrow 14^+$	$1.74^{+0.07}_{-0.08}$		0.55(5)		$19.79^{+0.90}_{-1.00} \times 10^{-4}$	
536.8	$16^- \rightarrow 15^-$	$0.29^{+0.02}_{-0.03}$	1.05(2)	0.13(1)	0.17	$0.71^{+0.05}_{-0.07}$	0.90
556.9	$17^- \rightarrow 16^-$		1.25(4)	0.11(1)	0.23	>0.16	1.06

Table 3. The calculated shell-model wave functions corresponding to different excited states in ^{92}Mo. Wave functions are presented in the form $P = [\pi(p(1), p(2), p(3), p(4)) \otimes \nu\ (n(1), n(2), n(3), n(4))]$, where $p(i)$ represents the number of protons in $f_{5/2}$, $p_{3/2}$, $p_{1/2}$, and $g_{9/2}$ orbits, and $n(i)$ represents the number of neutrons in $g_{9/2}$, $d_{5/2}$, $g_{7/2}$, and $s_{1/2}$ orbits, respectively.

State	Energy (MeV)	Probability	Configuration
0_1^+	0.000	33.4%	$\pi(6\,4\,2\,2) \otimes \nu(10\,0\,0\,0)$
		24.8%	$\pi(6\,4\,0\,4) \otimes \nu(10\,0\,0\,0)$
		14.5%	$\pi(6\,2\,2\,4) \otimes \nu(10\,0\,0\,0)$
2_1^+	1.683	25.5%	$\pi(6\,4\,0\,4) \otimes \nu(10\,0\,0\,0)$
		25.4%	$\pi(6\,4\,2\,2) \otimes \nu(10\,0\,0\,0)$
		12.6%	$\pi(4\,4\,2\,4) \otimes \nu(10\,0\,0\,0)$
4_1^+	2.644	34.0%	$\pi(6\,4\,2\,2) \otimes \nu(10\,0\,0\,0)$
		25.2%	$\pi(6\,4\,0\,4) \otimes \nu(10\,0\,0\,0)$
		11.5%	$\pi(6\,2\,2\,4) \otimes \nu(10\,0\,0\,0)$
6_1^+	2.888	40.2%	$\pi(6\,4\,2\,2) \otimes \nu(10\,0\,0\,0)$
		25.1%	$\pi(6\,4\,0\,4) \otimes \nu(10\,0\,0\,0)$
		10.0%	$\pi(6\,2\,2\,4) \otimes \nu(10\,0\,0\,0)$
4_2^+	2.951	31.1%	$\pi(6\,4\,0\,4) \otimes \nu(10\,0\,0\,0)$
		18.6%	$\pi(4\,4\,2\,4) \otimes \nu(10\,0\,0\,0)$
		17.8%	$\pi(5\,4\,1\,4) \otimes \nu(10\,0\,0\,0)$
8_1^+	3.093	41.7%	$\pi(6\,4\,2\,2) \otimes \nu(10\,0\,0\,0)$
		26.7%	$\pi(6\,4\,0\,4) \otimes \nu(10\,0\,0\,0)$
		10.6%	$\pi(6\,2\,2\,4) \otimes \nu(10\,0\,0\,0)$
10_1^+	4.773	33.6%	$\pi(6\,4\,0\,4) \otimes \nu(10\,0\,0\,0)$
		21.8%	$\pi(5\,4\,1\,4) \otimes \nu(10\,0\,0\,0)$
		16.5%	$\pi(4\,4\,2\,4) \otimes \nu(10\,0\,0\,0)$
12_1^+	5.872	46.2%	$\pi(6\,4\,0\,4) \otimes \nu(10\,0\,0\,0)$
		13.8%	$\pi(5\,4\,1\,4) \otimes \nu(10\,0\,0\,0)$
		12.4%	$\pi(4\,4\,2\,4) \otimes \nu(10\,0\,0\,0)$
12_2^+	6.470	63.0%	$\pi(5\,4\,1\,4) \otimes \nu(10\,0\,0\,0)$
		11.2%	$\pi(5\,3\,2\,4) \otimes \nu(10\,0\,0\,0)$
13_1^+	6.660	72.8%	$\pi(5\,4\,1\,4) \otimes \nu(10\,0\,0\,0)$
		12.9%	$\pi(5\,3\,2\,4) \otimes \nu(10\,0\,0\,0)$
15_1^+	7.426	74.6%	$\pi(5\,4\,1\,4) \otimes \nu(10\,0\,0\,0)$
		12.6%	$\pi(5\,3\,2\,4) \otimes \nu(10\,0\,0\,0)$
14_1^+	7.521	57.0%	$\pi(5\,4\,1\,4) \otimes \nu(10\,0\,0\,0)$
		18.9%	$\pi(5\,3\,2\,4) \otimes \nu(10\,0\,0\,0)$
14_2^+	7.678	68.8%	$\pi(5\,4\,1\,4) \otimes \nu(10\,0\,0\,0)$
		15.0%	$\pi(5\,3\,2\,4) \otimes \nu(10\,0\,0\,0)$
13_2^+	7.690	56.6%	$\pi(6\,4\,2\,2) \otimes \nu(9\,1\,0\,0)$
		13.4%	$\pi(6\,4\,0\,4) \otimes \nu(9\,1\,0\,0)$

experimental 4^+ state as the shell-model predicted 4_1^+ state. However, the model was not able to produce appropriate B(E2) for the $4_1^+ \rightarrow 2_1^+$ value. The theoretically predicted 6^+ and 8^+ states have similar mixed configurations of $\pi(f_{5/2}^6 p_{3/2}^4 p_{1/2}^2 g_{9/2}^2) \otimes \nu(g_{9/2}^{10})$, $\pi(f_{5/2}^6 p_{3/2}^4 p_{1/2}^0 g_{9/2}^4) \otimes \nu(g_{9/2}^{10})$, and $\pi(f_{5/2}^6 p_{3/2}^2 p_{1/2}^2 g_{9/2}^4) \otimes \nu(g_{9/2}^{10})$. We interpreted the 8^+ state as a maximum aligned state whose spin is generated from two unpaired protons in the $g_{9/2}$ orbital.

Table 4. Continued from table 3.

State	Energy (MeV)	Probability	Configuration
14_3^+	8.275	61.4%	$\pi(6\,4\,2\,2) \otimes \nu(9\,1\,0\,0)$
		15.2%	$\pi(6\,4\,0\,4) \otimes \nu(9\,1\,0\,0)$
15_2^+	8.886	61.1%	$\pi(6\,4\,2\,2) \otimes \nu(9\,1\,0\,0)$
		15.1%	$\pi(6\,4\,0\,4) \otimes \nu(9\,1\,0\,0)$
15_3^+	9.129	68.0%	$\pi(5\,4\,1\,4) \otimes \nu(9\,1\,0\,0)$
		13.7%	$\pi(5\,3\,2\,4) \otimes \nu(9\,1\,0\,0)$
16_1^+	9.646	65.4%	$\pi(5\,4\,1\,4) \otimes \nu(9\,1\,0\,0)$
		14.9%	$\pi(5\,4\,1\,4) \otimes \nu(9\,0\,0\,1)$
		11.2%	$\pi(5\,3\,2\,4) \otimes \nu(9\,1\,0\,0)$
16_2^+	9.791	55.4%	$\pi(5\,4\,1\,4) \otimes \nu(9\,1\,0\,0)$
		14.6%	$\pi(5\,3\,2\,4) \otimes \nu(9\,1\,0\,0)$
17_1^+	10.207	71.2%	$\pi(5\,4\,1\,4) \otimes \nu(9\,1\,0\,0)$
		14.1%	$\pi(5\,3\,2\,4) \otimes \nu(9\,1\,0\,0)$
18_1^+	10.835	71.4%	$\pi(5\,4\,1\,4) \otimes \nu(9\,1\,0\,0)$
		14.4%	$\pi(5\,3\,2\,4) \otimes \nu(9\,1\,0\,0)$
19_1^+	11.390	67.0%	$\pi(5\,4\,1\,4) \otimes \nu(9\,1\,0\,0)$
		14.4%	$\pi(5\,3\,2\,4) \otimes \nu(9\,1\,0\,0)$
19_2^+	11.458	76.4%	$\pi(5\,4\,1\,4) \otimes \nu(9\,0\,1\,0)$
		10.0%	$\pi(5\,3\,2\,4) \otimes \nu(9\,0\,1\,0)$
20_1^+	12.092	74.2%	$\pi(5\,4\,1\,4) \otimes \nu(9\,0\,1\,0)$
		11.8%	$\pi(5\,3\,2\,4) \otimes \nu(9\,0\,1\,0)$
20_2^+	12.204	66.0%	$\pi(5\,4\,1\,4) \otimes \nu(9\,1\,0\,0)$
		18.5%	$\pi(5\,3\,2\,4) \otimes \nu(9\,1\,0\,0)$
21_1^+	12.471	75.9%	$\pi(5\,4\,1\,4) \otimes \nu(9\,1\,0\,0)$
		19.6%	$\pi(5\,3\,2\,4) \otimes \nu(9\,1\,0\,0)$
5_1^-	2.692	73.8%	$\pi(6\,4\,1\,3) \otimes \nu(10\,0\,0\,0)$
7_1^-	3.615	40.4%	$\pi(6\,4\,1\,3) \otimes \nu(10\,0\,0\,0)$
		24.8%	$\pi(5\,4\,2\,3) \otimes \nu(10\,0\,0\,0)$
9_1^-	4.546	69.9%	$\pi(6\,4\,1\,3) \otimes \nu(10\,0\,0\,0)$
11_1^-	4.842	77.9%	$\pi(6\,4\,1\,3) \otimes \nu(10\,0\,0\,0)$
13_1^-	6.456	49.8%	$\pi(5\,4\,0\,5) \otimes \nu(10\,0\,0\,0)$
		19.4%	$\pi(5\,4\,2\,3) \otimes \nu(10\,0\,0\,0)$
12_1^-	6.866	52.4%	$\pi(5\,4\,2\,3) \otimes \nu(10\,0\,0\,0)$
		24.3%	$\pi(5\,4\,0\,5) \otimes \nu(10\,0\,0\,0)$
15_1^-	7.734	55.2%	$\pi(5\,4\,0\,5) \otimes \nu(10\,0\,0\,0)$
		16.9%	$\pi(5\,3\,1\,5) \otimes \nu(10\,0\,0\,0)$
		11.3%	$\pi(4\,4\,1\,5) \otimes \nu(10\,0\,0\,0)$
14_1^-	8.640	43.1%	$\pi(5\,4\,0\,5) \otimes \nu(10\,0\,0\,0)$
		22.0%	$\pi(4\,4\,1\,5) \otimes \nu(10\,0\,0\,0)$
		10.3%	$\pi(5\,3\,1\,5) \otimes \nu(10\,0\,0\,0)$

To produce higher spin states, the breaking of a pair in the $g_{9/2}$ orbital is required. The experimentally observed 10^+ and 12_1^+ states essentially originate from the $\pi(f_{5/2}^6 p_{3/2}^4 p_{1/2}^0 g_{9/2}^4) \otimes \nu(g_{9/2}^{10})$ configuration with ν=4. This band terminates at the maximum aligned 12_1^+ state. On top of the experimental 12_1^+ state, we observed several high-

Table 5. Continued from table 4.

State	Energy (MeV)	Probability	Configuration
14_2^-	8.936	42.6%	$\pi(5\,4\,2\,3)\otimes\nu(9\,1\,0\,0)$
		32.6%	$\pi(6\,4\,1\,3)\otimes\nu(9\,1\,0\,0)$
15_2^-	8.959	45.0%	$\pi(4\,4\,1\,5)\otimes\nu(10\,0\,0\,0)$
		13.0%	$\pi(5\,3\,1\,5)\otimes\nu(10\,0\,0\,0)$
		12.3%	$\pi(5\,4\,0\,5)\otimes\nu(10\,0\,0\,0)$
15_3^-	9.301	37.8%	$\pi(5\,4\,0\,5)\otimes\nu(9\,1\,0\,0)$
		25.4%	$\pi(5\,4\,0\,5)\otimes\nu(9\,0\,0\,1)$
		10.5%	$\pi(5\,4\,2\,3)\otimes\nu(9\,1\,0\,0)$
15_4^-	9.376	58.7%	$\pi(6\,4\,1\,3)\otimes\nu(9\,1\,0\,0)$
		24.2%	$\pi(5\,4\,2\,3)\otimes\nu(9\,1\,0\,0)$
16_1^-	9.827	37.3%	$\pi(5\,4\,2\,3)\otimes\nu(9\,1\,0\,0)$
		30.9%	$\pi(5\,4\,0\,5)\otimes\nu(9\,1\,0\,0)$
17_1^-	9.882	62.2%	$\pi(4\,4\,1\,5)\otimes\nu(10\,0\,0\,0)$
		10.0%	$\pi(4\,3\,2\,5)\otimes\nu(10\,0\,0\,0)$
16_2^-	9.972	70.8%	$\pi(6\,4\,1\,3)\otimes\nu(9\,1\,0\,0)$
		10.3%	$\pi(5\,4\,2\,3)\otimes\nu(9\,1\,0\,0)$
17_2^-	10.281	48.0%	$\pi(5\,4\,2\,3)\otimes\nu(9\,1\,0\,0)$
		19.4%	$\pi(5\,4\,0\,5)\otimes\nu(9\,1\,0\,0)$
		10.6%	$\pi(6\,4\,1\,3)\otimes\nu(9\,1\,0\,0)$
17_3^-	10.478	61.9%	$\pi(6\,4\,1\,3)\otimes\nu(9\,1\,0\,0)$
		10.4%	$\pi(5\,4\,2\,3)\otimes\nu(9\,1\,0\,0)$
18_1^-	10.915	66.7%	$\pi(6\,4\,1\,3)\otimes\nu(9\,1\,0\,0)$
		14.9%	$\pi(5\,4\,2\,3)\otimes\nu(9\,1\,0\,0)$
19_1^-	11.503	39.3%	$\pi(5\,4\,0\,5)\otimes\nu(9\,1\,0\,0)$
		32.2%	$\pi(5\,4\,2\,3)\otimes\nu(9\,1\,0\,0)$
19_2^-	11.589	59.8%	$\pi(5\,4\,0\,5)\otimes\nu(9\,0\,1\,0)$
		11.8%	$\pi(5\,3\,1\,5)\otimes\nu(9\,0\,1\,0)$
		11.6%	$\pi(4\,4\,1\,5)\otimes\nu(9\,0\,1\,0)$
20_1^-	12.003	24.7%	$\pi(5\,4\,2\,3)\otimes\nu(9\,1\,0\,0)$
		23.6%	$\pi(5\,4\,0\,5)\otimes\nu(9\,1\,0\,0)$
		22.6%	$\pi(5\,4\,0\,5)\otimes\nu(9\,0\,1\,0)$
20_2^-	12.071	36.9%	$\pi(5\,4\,0\,5)\otimes\nu(9\,0\,1\,0)$
		19.6%	$\pi(5\,4\,2\,3)\otimes\nu(9\,1\,0\,0)$
		11.9%	$\pi(5\,4\,0\,5)\otimes\nu(9\,1\,0\,0)$

energy transitions, namely, 2059.7, 2075.7, and 2360.8 keV. The energy levels at 7921.1, 7936.8, and 8220.9 keV (see figure 1) can be interpreted as theoretically predicted 14_3^+, 13_2^+, and 14_1^- states, respectively. The dominant configurations of the shell-model predicted 13_2^+, 14_3^+, and 14_1^- states are $\pi(f_{5/2}^6 p_{3/2}^4 p_{1/2}^2 g_{9/2}^2)\otimes\nu(g_{9/2}^9 d_{5/2}^1)$, $\pi(f_{5/2}^6 p_{3/2}^4 p_{1/2}^2 g_{9/2}^2)\otimes\nu(g_{9/2}^9 d_{5/2}^1)$ and $\pi(f_{5/2}^5 p_{3/2}^4 p_{1/2}^0 g_{9/2}^5)\otimes\nu(g_{9/2}^{10})$, respectively. These high-energy γ rays reflect either proton or neutron core excitation. The 13_2^+, and 14_3^+ states can be pictured as coupling of two stretched proton and neutron configurations, namely, $\pi[f_{5/2}^6 p_{3/2}^4 p_{1/2}^2 g_{9/2}^2]_{8^+}$ and $\nu[g_{9/2}^9 d_{5/2}^1]_{7^+}$. The 8^+ state at 2760.2 keV energy has a fully aligned structure with the $\pi(f_{5/2}^6 p_{3/2}^4 p_{1/2}^2 g_{9/2}^2)\otimes\nu(g_{9/2}^{10})$ configuration. The energy difference between $14^{(+)}$ and 8^+ is ≈5.2 MeV. This indicates the breaking of a proton's pair in the

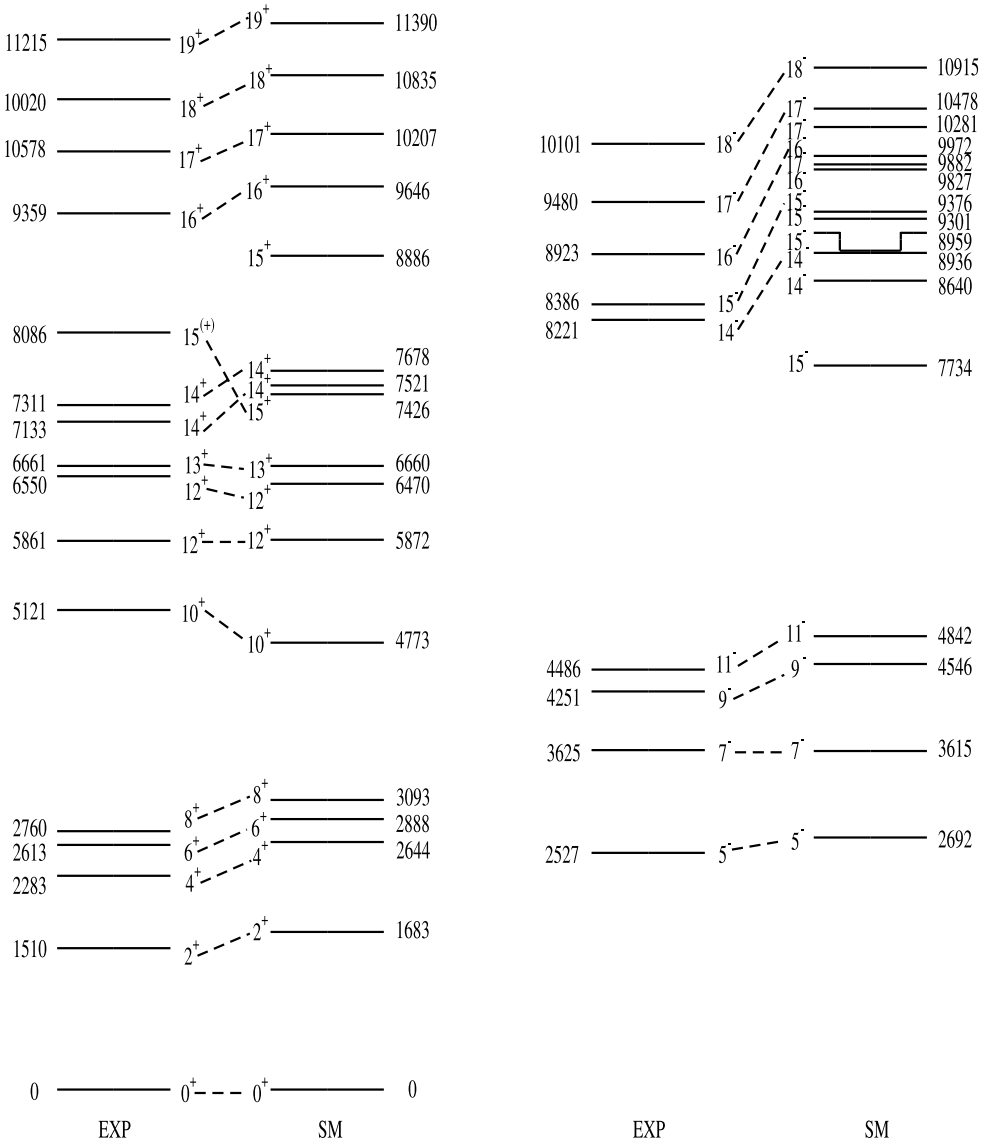

Figure 8. Comparisons of experimental levels and shell-model calculated levels using GWBXG interaction. Only those experimental and the corresponding assigned theoretically predicted energy levels are shown whose spin-parity is confined. All shown energies are in keV and rounded to their nearest integer, as given in figure 1 and table 1.

$g_{9/2}$ orbital and simultaneous neutron excitation from the $g_{9/2}$ to the $d_{5/2}$ orbital. Similar excitation has been observed in N = 50 isotones, ^{93}Tc [16], and ^{94}Ru [16]. In [16], ROTH *et al* reported that the states from $19/2^+$ to $39/2^+$ and 12^+ to 19^+ primarily originate from neutron particle-hole excitation $\nu[g^9_{9/2}d^1_{5/2}]_{7^+}$ coupled to $\pi(f^6_{5/2}p^4_{3/2}p^2_{1/2}g^n_{9/2})$ (where n=3,4 for ^{93}Tc and ^{94}Ru, respectively) in ^{93}Tc and ^{94}Ru, respectively. Simultaneous excitation of

protons and neutrons across the $Z = 40$ and $N = 50$ shells, respectively, was responsible for generating those states.

The experimental states at 6550.4 keV and 6661.2 keV are assigned as 12^+ and 13^+, respectively, conflicting with previous studies [12, 13, 15, 45]. The shell-model prediction decently reproduced the level energies of these states.

The positive-parity 12_2^+, 13_1^+, 14_1^+, 14_2^+, and $15^{(+)}$ states mainly stem from the $\pi(f_{5/2}^5 p_{3/2}^4 p_{1/2}^1 g_{9/2}^4) \otimes \nu(g_{9/2}^{10})$ configuration with $\nu = 6$. The $15^{(+)}$ state is a maximum aligned state. However, the shell-model result predicts that the energy of the 15^+ state is even lower than that of the 14_1^+ state. The experimental 8380.1 keV energy level can be interpreted as the theoretically predicted 14_4^+ state with $\pi(f_{5/2}^6 p_{3/2}^3 p_{1/2}^1 g_{9/2}^4) \otimes \nu(g_{9/2}^{10})$ as a dominant configuration.

To generate positive-parity states higher than $I = 15\hbar$, neutron core excitation is required. The states in Band I are essentially generated from neutron core excitation across the $N = 50$ shell gap. The suggested dominant configuration of states from 16^+ to 19^+ is $\pi(f_{5/2}^5 p_{3/2}^4 p_{1/2}^1 g_{9/2}^4) \otimes \nu(g_{9/2}^9 d_{5/2}^1)$.

For positive spin, the configurations mainly change after spin 8^+, 12^+, and 15^+. These configurations are either core excitation across Z = 38 or 40 shell, or N = 50 core excitation.

4.2. Negative-parity states

Shell-model calculation predicts negative-parity states from 5^- to 11^-, mainly stemming from the $\pi(f_{5/2}^6 p_{3/2}^4 p_{1/2}^1 g_{9/2}^3) \otimes \nu(g_{9/2}^{10})$ configuration. Except for 5^- , all of the other three levels have seniority $\nu = 4$. This band terminates at the fully aligned 11^- state. Similar to the 12_1^+ state, neutron-or proton core excitation is required to produce higher states than 11^-.

For Band II and 14^- (see level scheme 1), the B(M1) values are used to assign the configuration. The adopted B(M1) values among different transition possibilities are 0.148, 1.615, 1.898, and 0.423 μ_N^2 for $15_4^- \rightarrow 14_2^-$, $16_2^- \rightarrow 15_4^-$, $17_3^- \rightarrow 16_2^-$, and $18_1^- \rightarrow 17_3^-$, respectively. The shell-model calculation suggests that experimental 14^- emerges from a configuration of $\pi(f_{5/2}^5 p_{3/2}^4 p_{1/2}^2 g_{9/2}^3) \otimes \nu(g_{9/2}^9 d_{5/2}^1)$ mixed with $\pi(f_{5/2}^6 p_{3/2}^4 p_{1/2}^1 g_{9/2}^3) \otimes \nu(g_{9/2}^9 d_{5/2}^1)$, with seniority of $\nu = 4$ and 6, respectively. The states in Band II are dominated by the $\pi(f_{5/2}^6 p_{3/2}^4 p_{1/2}^1 g_{9/2}^3) \otimes \nu(g_{9/2}^9 d_{5/2}^1)$ configuration. Similar to Band I, this band is also constructed from the coupling of the almost stretched configuration of protons and neutrons. Table 6 represents the energy difference between the aligned proton state coupled with the neutron core-excited structure $\nu(g_{9/2}^9 d_{5/2}^1)$ and the aligned proton state for N = 50 nuclei. In ^{91}Nb, the maximum aligned state with the$[\pi(f_{5/2}^6 p_{3/2}^4 p_{1/2}^0 g_{9/2}^3) \otimes \nu(g_{9/2}^9 d_{5/2}^1)]_{35/2^+}$ configuration was not observed [17]. Therefore, the maximum experimental observed spin of this configuration was taken for comparison [17]. However, since we calculated the energy difference normalized with the spin difference (Δe), we can compare the results on the same scale. The values are remarkably constant with a mean value $\approx$785 keV/$\hbar$.

4.3. Lifetime of dipole transitions

We estimated the lifetime of 17^-, 16^-, 15^-, and 14_2^+ states from the theoretical calculations. A comparison of the theoretical and experimental lifetime at this high spin can provide an intriguing platform to test the shell model. The theoretically predicted lifetime (τ_{th}) is shown in table 2. The 14^+ state's lifetime was overpredicted by $\sim$0.5 ps. The calculations show a reasonable agreement of the experimental lifetime for 16^- states with an underprediction of approximately 0.17 ps. On the other hand, the theoretical life of the 15^- state cannot be

Table 6. The relative energy difference between proton aligned states in N = 50 isotones (^{90}Zr, ^{91}Nb, ^{92}Mo, ^{93}Tc, ^{94}Ru, and ^{95}Rh) with respect to the state with both proton and neutron alignment. Wave functions are presented in the form $P = \nu[\pi(p(1), p(2), p(3), p(4))\otimes\nu(n(1), n(2))]$, where $p(i)$ represents the number of protons in $f_{5/2}$, $p_{3/2}$, $p_{1/2}$, and $g_{9/2}$ orbits and $n(i)$ represents the number of neutrons in $g_{9/2}$, and $d_{5/2}$ orbits, respectively. All level energies are rounded off to their nearest integer, as given in [3, 16, 17] and table 1.

Mass no.	$I_i^\pi \rightarrow I_f^\pi$	E_i (keV)	E_f (keV)	Configuration of I_i	Configuration of I_f	$\Delta e = \frac{E_f - E_i}{I_i^\pi - I_f^\pi}$ (keV/$\hbar$)
90[a]	$15^+ \rightarrow 8^+$	8955	3588	π(6 4 0 2)$\otimes\nu$(9 1)	π(6 4 0 2)$\otimes\nu$(10 0)	767
91[a]	$31/2^+ \rightarrow 21/2^+$	7438	3467	π(6 4 0 3)$\otimes\nu$(9 1)	π(6 4 03)$\otimes\nu$(10 0)	794
92[b]	$18^- \rightarrow 11^-$	10 101	4486	π(6 4 1 3)$\otimes\nu$(9 1)	π(6 4 1 3)$\otimes\nu$(10 0)	802
93[a]	$39/2^- \rightarrow 25/2^-$	9420	3887	π(6 4 1 4)$\otimes\nu$(9 1)	π(6 4 1 4)$\otimes\nu$(10 0)	790
94[a]	$20^- \rightarrow 13^-$	11 040	5568	π(6 4 1 5)$\otimes\nu$(9 1)	π(6 4 1 5)$\otimes\nu$(10 0)	782
95[a]	$39/2^- \rightarrow 25/2^-$	9346	3908	π(6 4 1 6)$\otimes\nu$(9 1)	π(6 4 1 6)$\otimes\nu$(10 0)	777

[a] Values taken from [3], [17], and [16], respectively.
[b] Current work.

Table 7. The B(E1) of E1 transition energies in ^{92}Mo.

E_γ (keV)	$I_i^\pi \rightarrow I_f^\pi$	Mean lifetime (τ) (ps)	B(E1) $\times 10^{-4}$ (W.u.)
244.0	$5^- \rightarrow 4^+$	2270(30)[a]	1.45(2)
85.2	$6^+ \rightarrow 5^-$	2200(20)[a]	2.97(41)
1491.0	$9^- \rightarrow 8^+$	37(11)[a]	0.012(4)
1375.0	$12^+ \rightarrow 11^-$	50(4)[b]	0.104(14)
2064.4	$12^+ \rightarrow 11^-$	<0.7[b]	> 5.43
1075.1	$15^- \rightarrow 14^+$	$1.74^{+0.07}_{-0.08}$[b]	$19.79^{+0.90}_{-1.00}$

[a] Values taken from [46] and [37], respectively.
[b] Current work.

calculated due to the limitations of available orbits. Additionally, the calculated lifetime of the 17^- state also falls under the limit. The B(M1) of the 649.6-, 536.8-, and 556.9 keV transitions is shown in table 2. The present study only provided a lower limit for the B(M1) of the 556.9 keV transition.

4.4. E1 transitions

The B(E1) value of E1 transitions is shown in table 7. The E1 transition operator connects orbitals that differ by orbital angular momentum $\Delta l = 1$ and total angular momentum $\Delta j \leqslant 1$. As mentioned in [15], the inclusion of orbitals above the $Z = N = 50$ core excitation and $Z = 28$ core breaking is required to fully explain the observed B(E1) values. Consequently, in our shell-model calculation using the GWBXG interaction, the E1 transition is forbidden.

The transition strength of the $15^- \rightarrow 14^+$ transition found in this work is comparatively very large relative to other E1 transitions. This kind of enhancement in the transition strength of the E1 transition was also observed in ^{94}Ru [18]. The enhanced E1 transition, $13^+ \rightarrow 12^-$, in ^{94}Ru has a B(E1) value of $2.2(4) \times 10^{-3}$ W.u. [18], which is of the same order as our measured B(E1) for the $15^- \rightarrow 14^+$ transition. In ^{94}Ru, the 13^+ state, dominated by $\nu(1d^1_{5/2}0g^{-1}_{9/2})$, is the neutron core-excited state on the positive-parity side [18]. The strongest E1 transition observed is from 13^+ to 12^-. The 12^- state contains a significant contribution from $1p_{3/2}$ proton excitation [18]. The involvement of proton and neutron core excitations mutually enhanced this E1 transition [18]. Similarly, the 1075.1 keV transition in ^{92}Mo also originates from a neutron core-excited state. Therefore, qualitatively, we can predict that the 1075.1 keV transition may be mutually enhanced by neutron and proton excitations.

5. Conclusion

We have studied the level scheme of ^{92}Mo with the ^{30}Si + ^{65}Cu fusion-evaporation reaction. The level scheme has been modified on the basis of our R_{ADO} and Δ_{asym} measurements. We identified the 2064.4 keV and 472.1 keV γ transitions at 6550.4 keV and 7133.3 keV energy levels as E1 and M1 in nature, respectively. This has led to a change in the tentatively assigned parity of the 6550.4 keV, 6661.2 keV, 7310.2 keV, 8386.2 keV, 8923.0 keV, 9479.8 keV, and 10 100.7 keV energy levels. Additionally, we determined that the multipolarity of the 2047.6 keV transition, which was earlier assigned as E1, is E2.

Large-scale shell-model calculations have been performed using the GWBXG interaction. These provided a good description of both positive- and negative-parity states. A comparison

between experimental levels and the calculated shell-model levels reveals the importance of $Z = 38$ and $N = 50$ core excitation in building the high-spin states. States above the 7310.9 keV energy level can be explained only through the coupling of the stretched proton and neutron core excitations. The positive- and negative-parity high-spin states of ^{92}Mo mainly originate from $\pi(f^5_{5/2}p^4_{3/2}p^1_{1/2}g^4_{9/2}) \otimes \nu(g^9_{9/2}d^1_{5/2})$ or $\pi(f^6_{5/2}p^4_{3/2}p^2_{1/2}g^2_{9/2}) \otimes \nu(g^9_{9/2}d^1_{5/2})$ and $\pi(f^6_{5/2}p^4_{3/2}p^1_{1/2}g^3_{9/2}) \otimes \nu(g^9_{9/2}d^1_{5/2})$ configurations, respectively. The energy required in the $N = 50$ nuclei to form a $\nu(g^9_{9/2}d^1_{5/2})$ particle-hole pair of spin $7\hbar$ and align with the proton structure of maximal spin is ≈5.50 MeV. A relatively large B(E1) of 1075.1 keV transition can be understood via the mutual enhancement of proton and neutron excitation.

Acknowledgments

The authors express their gratitude to the PLF staff for maintaining a stable beam throughout the experiment. Additionally, they acknowledge the assistance provided by S Jadhav, B Naidu, A T Vazhappilly, and R Donthi during the experiment. This work is funded by the Department of Atomic Energy, Government of India (Project Identification Code: 12-R&D-TFR-5.02-0200) and the Department of Science and Technology, Government of India (Grant No. IR/S2/PF-03/2003-II). P.C.S. acknowledges a research grant from SERB (India), CRG/2022/005167. U.G's work has been supported in part by the U.S. National Science Foundation (Grant Nos. PHY-2011890 and PHY-2310059).

Data availability statement

The data cannot be made publicly available upon publication because no suitable repository exists for hosting data in this field of study. The data that support the findings of this study are available upon reasonable request from the authors.

ORCID iDs

Vishal Malik https://orcid.org/0009-0000-6756-4335
R Palit https://orcid.org/0000-0001-9564-5431
Deepak Patel https://orcid.org/0000-0002-7669-1907
Somnath Nag https://orcid.org/0000-0002-0477-9061

References

[1] Saha S *et al* 2019 *Phys. Rev.* C **99** 054301
[2] Laskar M S R *et al* 2021 *Phys. Rev.* C **104** L011301
[3] Dey P *et al* 2022 *Phys. Rev.* C **105** 044307
[4] Saha S *et al* 2012 *Phys. Rev.* C **86** 034315
[5] Balanda A, Kulessa R, Walus W and Stachura Z 1978 *Acta Physica Polonica Series* B **9** 995–1001 (https://www.actaphys.uj.edu.pl/R/9/11/995/pdf)
[6] Lederer C M, Jaklevic J M and Hollander J M 1971 *Nucl. Phys.* A **169** 449–88
[7] Fields C A, Ristinen R A, Samuelson L E and Smith P A 1982 *Nucl. Phys.* A **385** 449–60
[8] Winter G *et al* 1993 *Phys. Rev.* C **48** 1010–9
[9] Käubler L *et al* 2002 *Phys. Rev.* C **65** 054315

[10] Stefanova E A, Schwengner R, Reif J, Schnare H, Dönau F, Wilhelm M, Fitzler A, Kasemann S, von Brentano P and Andrejtscheff W 2000 *Phys. Rev.* C **62** 054314
[11] Li Z Q *et al* 2016 *Phys. Rev.* C **94** 014315
[12] Singh P, Pillay R G, Sheikh J A and Devare H G 1992 *Phys. Rev.* C **45** 2161–71
[13] Pattabiraman N S, Chintalapudi S N, Ghugre S S, Tirumala Rao B V, Raju M L N, Reddy T S, Joshi P K, Palit R and Jain H C 2002 *Phys. Rev.* C **65** 044324
[14] Ghugre S S and Datta S K 1995 *Phys. Rev.* C **52** 1881–93
[15] Huang Z *et al* 2022 *Phys. Rev.* C **106** 064331
[16] Roth H A, Arnell S E, Foltescu D, Skeppstedt Ö, Blomqvist J, Nilsson A, Kuroyanagi T, Mitarai S and Nyberg J 1994 *Phys. Rev.* C **50** 1330–45
[17] Dey P, Palit R, Srivastava P C, Das B, Kundu A, Laskar M S R, Malik V, Negi D and Sharma S 2024 *Phys. Rev.* C **109** 034313
[18] Ghazi Moradi F *et al* 2014 *Phys. Rev.* C **89** 014301
[19] Ghazi Moradi F *et al* 2014 *Phys. Rev.* C **89** 044310
[20] Palit R 2011 *Application of Accelerators in Research and Industry Twenty-First International ConferenceAIP Conf. Proc. No. 1336* ed F D McDaniel and B L Doyle (AIP) p 573
[21] Palit R *et al* 2012 *Nucl. Instrum. Methods Phys. Res. Sect.* A **680** 90–6
[22] Radford D C 1995 *Nucl. Instrum. Methods Phys. Res., Sect.* A **361** 297–305
[23] Radford D C 1995 *Nucl. Instrum. Methods Phys. Res., Sect.* A **361** 306–16
[24] Northcliffe L C and Schilling R F 1970 *At. Data Nucl. Data Tables* **7** 233–463
[25] Das S *et al* 2017 *Nucl. Instrum. Methods Phys. Res., Sect.* A **841** 17–23
[26] Piiparinen M *et al* 1996 *Nucl. Phys.* A **605** 191–268
[27] Arnell S E, Foltescu D, Roth H A, Skeppstedt O ¨, Nilsson A, Mitarai S and Nyberg J 1992 *Phys. Scr.* **46** 389
[28] Singh P, Palit R, Saha S, Sethi J, Biswas S, Choudhury D, Srivastava P C and Trivedi T 2014 *Phys. Rev.* C **90** 014306
[29] Saha S *et al* 2012 *Phys. Rev.* C **86** 034315
[30] Saha S, Palit R, Sethi J, Biswas S, Singh P, Trivedi T, Choudhury D and Srivastava P C 2014 *Phys. Rev.* C **89** 044315
[31] Ray S, Pattabiraman N S, Goswami R, Ghugre S S, Sinha A K and Garg U 2004 *Phys. Rev.* C **69** 054314
[32] Jones P M, Wei L, Beck F A, Butler P A, Byrski T, Duchêne G, De France G, Hannachi F, Jones G D and Kharraja B 1995 *Nucl. Instrum. Methods Phys. Res. Sect.* A **362** 556–60
[33] www.srim.org.
[34] Saha S *et al* 2019 *Phys. Rev.* C **99** 054301
[35] Kundu A *et al* 2021 *Phys. Rev.* C **103** 034315
[36] Babra F S *et al* 2021 *Phys. Rev.* C **103** 014316
[37] Baglin C M 2012 *Nucl. Data Sheets* **113** 2187–389
[38] Das P, Pillay R G and Devare H G 1994 *Phys. Rev.* C **50** 1219–21
[39] Hosaka A, Kubo K-I and Toki H 1985 *Nucl. Phys.* A **444** 76–92
[40] Ji X and Wildenthal B H 1988 *Phys. Rev.* C **37** 1256–66
[41] Gloeckner D H 1975 *Nucl. Phys.* A **253** 301–23
[42] Serduke F J D, Lawson R D and Gloeckner D H 1976 *Nucl. Phys.* A **256** 45–86
[43] Shimizu N, Mizusaki T, Utsuno Y and Yusuke T 2019 *Comput. Phys. Commun.* **244** 372–84
[44] Pérez-Vidal R M *et al* 2022 *Phys. Rev. Lett.* **129** 112501
[45] Fukuchi T *et al* 2005 *Eur. Phys. J. A-Hadrons and Nuclei* **24** 249–57
[46] Ley M, Knafla L, Jolie J, Esmaylzadeh A, Harter A, Blazhev A, Fransen C, Pfeil A, Régis J-M and Isacker P V 2023 *Phys. Rev.* C **108** 064313